Formation of surface nanodroplets under controlled flow conditions

Xuehua Zhang[a,b,1], Ziyang Lu[a], Huanshu Tan[a,b], Lei Bao[a], Yinghe He[c], Chao Sun[b], and Detlef Lohse[b]

[a]School of Civil, Environmental and Chemical Engineering, Royal Melbourne Institute of Technology, Melbourne, VIC 3001, Australia; [b]Physics of Fluids Group, MESA+ Institute, and J. M. Burgers Centre for Fluid Dynamics, University of Twente, 7500 AE Enschede, The Netherlands; and [c]Centre for Biodiscovery and Molecular Development of Therapeutics, College of Science, Technology Engineering, James Cook University, Townsville City, QLD 4811, Australia

Edited by David A. Weitz, Harvard University, Cambridge, MA, and approved June 9, 2015 (received for review March 27, 2015)

Nanodroplets on a solid surface (i.e., surface nanodroplets) have practical implications for high-throughput chemical and biological analysis, lubrications, laboratory-on-chip devices, and near-field imaging techniques. Oil nanodroplets can be produced on a solid–liquid interface in a simple step of solvent exchange in which a good solvent of oil is displaced by a poor solvent. In this work, we experimentally and theoretically investigate the formation of nanodroplets by the solvent exchange process under well-controlled flow conditions. We find significant effects from the flow rate and the flow geometry on the droplet size. We develop a theoretical framework to account for these effects. The main idea is that the droplet nuclei are exposed to an oil oversaturation pulse during the exchange process. The analysis shows that the volume of the nanodroplets increases with the Peclet number *Pe* of the flow as $\propto Pe^{3/4}$, which is in good agreement with our experimental results. In addition, at fixed flow rate and thus fixed Peclet number, larger and less homogeneously distributed droplets formed at less-narrow channels, due to convection effects originating from the density difference between the two solutions of the solvent exchange. The understanding from this work provides valuable guidelines for producing surface nanodroplets with desired sizes by controlling the flow conditions.

surface nanodroplet | solvent exchange | flow condition | Peclet number | heterogeneous nucleation

Nanoscale droplets on a substrate (1) are an essential element for a wide range of applications, namely laboratory-on-chip devices, simple and highly efficient miniaturized reactors for concentrating products, high-throughput single-bacteria or single-biomolecular analysis, encapsulation, and high-resolution imaging techniques, among others (2–5). These droplets are of great interest also because they can have a payload and can flow internally in response to external flow. As a consequence, such droplets are widely exploited in formulation industries. Quite some effort has been devoted to produce a large amount of nanodroplets in a controlled way. The current techniques include trapping by microcavities, emulsion direct adsorption, microprinting, and others (6). The solvent exchange process is a simple and generic approach for producing droplets or bubbles at solid–liquid interfaces that are only several tens to hundreds of nanometers in height, or a few femtoliters in volume (7–11). The approach has attractive advantages, such as its capability of producing a large number of nanodroplets in one simple step, and its generality in chemical composition of the droplet liquid, and flexibility in aspect ratio of the droplets and spatial structure or size of the substrate (9, 12).

For the formation of surface nanodroplets by solvent exchange, a hydrophobic substrate is exposed sequentially to two miscible solutions of oil, where the second solvent has a lower solubility of oil than the first. Such solubility difference leads to supersaturation of the liquid with oil during the solvent exchange and consequently to the nucleation of nanodroplets on the substrate. The analog technique in a bulk system is called solvent shifting or nanoprecipitaion through the ouzo effect (13), which has been increasingly applied to obtain nanodroplets in a surfactant-free emulsion (14), and monodispersed polymeric nanoparticles with precisely controlled sizes (12, 15–17), or assemble colloidal particles on a microscale (18).

Although the chemical composition of the solutions has been used to adjust the average size of the droplets (12), the flow properties dramatically complicate the formation of nanodroplets by the solvent exchange. The reason is that the mixing of the two liquids strongly depends on the flow conditions (19, 20). Inspired by the pattern formation of mineral aggregates from liquid displacement under quasi-2D flow conditions (21, 22), we may be able to control the droplet nucleation and growth by the flow conditions in a well-defined flow system. In this work, we experimentally and theoretically investigate the effects of the flow conditions on the formation of surface nanodroplets. We find that the averaged volume of surface nanodroplets increases with the Peclet number as $\propto Pe^{3/4}$, in good agreement with the experiments. To our knowledge, this work is the first attempt to quantitatively understand the effects of the flow conditions during the solvent exchange on the formation of surface nanodroplets.

Results and Discussion

Droplet Volume Dependence on the Flow Rate. The geometry of the solvent exchange channel and process is shown in schematic drawings in Fig. 1*A*. Three fluid channels with different heights were used and their dimensions are listed in Table 1. During the solvent exchange process, solution A [50% (vol/vol) ethanol aqueous solution saturated with polymerizable oil, with high oil solubility] was displaced by solution B (oil-saturated water, with low oil solubility). The injection of solution B was performed at a

Significance

Solvent exchange is a generally used approach for producing many nanoscale droplets on an immersed substrate. In this process, a good solvent is displaced by a poor solvent of oil, leading to oil nanodroplet nucleation and subsequent growth on the substrate. This work is, to our knowledge, the first attempt to quantitatively understand the relationship between the droplet size and the flow conditions during the solvent exchange, and to pave the way for the droplet size control. The experimental results show that the droplet volume increases with increasing Peclet number of the flow as $\propto Pe^{3/4}$, in good agreement with our theoretical analysis. We also reveal that the buoyancy effects contribute to the formation of bigger and less homogeneously distributed droplets in less-narrow channels.

Author contributions: X.Z. designed research; X.Z., Z.L., L.B., Y.H., and D.L. performed research; X.Z., Z.L., H.T., C.S., and D.L. analyzed data; and X.Z. and D.L. wrote the paper.

The authors declare no conflict of interest.

This article is a PNAS Direct Submission.

[1]To whom correspondence should be addressed. Email: xuehua.zhang@rmit.edu.au.

This article contains supporting information online at www.pnas.org/lookup/suppl/doi:10.1073/pnas.1506071112/-/DCSupplemental.

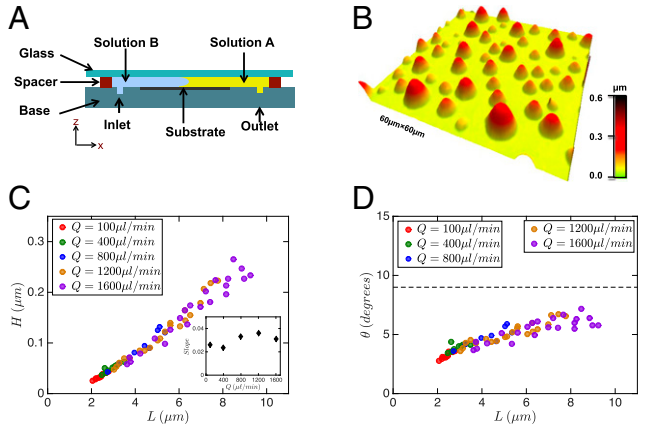

Fig. 1. Solvent exchange process and morphologic features of surface droplets formed at different flow rates for the narrow channel ($h = 0.33$ mm). (*A*) Schematic drawings of a fluid channel. The channel consists of a glass top window, a spacer, and a base. The hydrophobic substrate is placed inside the cell, facing the transparent glass window. The distance between the substrate and the glass bottom surface can be adjusted by the thickness of the spacer. The flow direction is in the x direction. (*B*) Representative AFM image of the polymerized droplets. (*C*) Droplet height H and (*D*) the contact angle θ versus the lateral diameter L of the nanodroplets. The macroscopic receding angle is shown for comparison. The slope in the height versus lateral extension curves in *C* is shown for a given flow rate in *C* (*Inset*). Clearly, it is nearly independent of the flow rate. Therefore, for given droplet size, also the contact angle is independent of the flow rate, as can be seen in *D*.

constant flow rate Q controlled by a syringe pump. Once the solvent exchange was completed, the nanodroplets on the substrate were cured by photopolymerization.

Fig. 1*B* shows a representative atomic force microscopy (AFM) image of the polymerized nanodroplets. The polymerized droplets are spherical caps with a certain size distribution. The plot in Fig. 1*C* shows that the droplet height increases monotonically from 10 to 300 nm as the lateral size increases from 2 μm up to 10 μm, consistent with the previous reports (9). The contact angles of those polymerized droplets lie below the macroscopic receding contact angles of the system. [Strictly speaking, the contact angle of a liquid droplet before the polymerization is about 1–2° larger than that of its polymerized counterpart due to curing shrinkage.]

As is known (23), the contact angle of droplets slightly depend on the droplet's lateral size, which holds for all flow rates. However, clearly the flow rate does not directly influence the contact angle of the surface nanodroplets.

The droplet volume is calculated from its lateral diameter in the optical images of the polymerized droplets in Fig. 2, and the corresponding relationship in Fig. 1*C*. Fig. 2*D* shows the probability distribution function (PDF) of the droplet volume at different flow rates in the narrowest channel, where the distribution of the droplet volume became wider at a faster flow rate. To further examine effects of the flow rate on the droplet size, we measured the lateral diameter of droplets that were produced from different flow rates at all three channels. The averaged lateral diameter of the droplets versus the flow rate is plotted in Fig. 2*E*, which shows a fast increase of the droplet size with an increase in the flow rate for all three channel heights. For instance, in the narrow channel the spatially averaged droplet diameter increased from 2 to 10 μm (20 to 300 nm in height) as the flow rate increased from 100 to 2,400 μL/min. The result shows the same trend for the two less-narrow channels, but the absolute values are larger on average.

We analyzed all droplet volumes *Vol* over a surface area of 0.35 mm^2 and obtained the averaged droplet volume per unit area of μm^2. The plot in Fig. 2*F* shows a sharp increase of the averaged droplet volume with increasing flow rate. The same data are shown in Fig. 2*G* (in a log–log plot) versus the Peclet number

$$Pe = \frac{\overline{U}h}{D} = \frac{Q}{wD} \quad [1]$$

of the flow, where D is the diffusion constant. The data can be described with the scaling law $Vol \propto Pe^{3/4}$. Later we will show that this scaling law between the droplet volume and the Pe number is in a good agreement with the theoretical prediction.

It is crucial to identify the formation mechanism of the droplets before we develop a theoretical model to understand the effect of the flow rate. In a tertiary system of ethanol–oil–water such as ours, surface nanodroplets may nucleate on the surface, or through the standard "ouzo effect," namely nucleate in the bulk liquid (13, 17, 24–26), and only later adsorb onto the surface. To find out which of the two processes is dominant, we analyzed the droplet volume and the surrounding droplet-depleted zone, following the modified Voronoi tessellation method in our previous work (27). In Figs. S1 and S2, we show the relation between the depleted area and the area of the corresponding footprint of nanodroplets produced at different flow rates. For the relatively large nanodroplets, the depleted area is proportional to the droplet footprint area. This correlation clearly suggests that surface nanodroplets are not from random adsorption of emulsion droplets formed in the bulk, but from heterogeneous nucleation and subsequent diffusion-driven growth. In this process, the oil dissolved in the bulk is (partly) consumed by the growing surface droplets, leading to the droplet-depleted area in the surrounding region. In contrast, the adsorption of bulk droplets to the surface could not give rise to the correlation between the droplet size and the depleted area. The same diffusion-driven mechanism and the same correlation between the depleted area and the footprint area was also observed (and derived) for the spatial arrangement of surface nanobubbles formed by the solvent exchange method (27).

Simple Theoretical Model

Mathematical Description of the Solvent Exchange Process. As shown in the schematic drawings of Fig. 1, the flow cell consists of a channel with height h and channel width w. The maximal flow velocity is U, and the mean flow velocity $\overline{U}$. The resulting flow rate is $Q = hw\overline{U}$, its Reynolds number $Re = \overline{U}h/\nu = Q/(w\nu)$. For the theory we will focus on laminar flow, i.e., $Re \lesssim 1$, which, as seen from Table 1, is justified for all channels. Furthermore, we will neglect the density contrast between the ethanol solution and the water (factor about 0.9), which, as we will see below,

Table 1. Experimental cases and parameters for different fluid channel heights *h*

			$\overline{U}$ (mm/s)		
Q (μL/min)	Re	Pe	h = 0.33 mm	h = 0.68 mm	h = 2.21 mm
100	0.04	119	0.36	0.18	0.05
200	0.09	238	0.72	0.35	0.11
400	0.18	476	1.44	0.70	0.22
600	0.27	714	2.16	1.05	0.32
800	0.35	952	2.88	1.40	0.43
1,200	0.53	1,429	4.32	2.10	0.65
1,600	0.71	1,905	5.77	2.80	0.86
2,400	1.06	2,857	8.66	4.20	1.29

For all cases the width of fluid channels w and the length l are 14 and 56 mm, respectively. Q is the flow rate, $\overline{U} = Q/(wh)$ the mean flow velocity, $Re = \overline{U}h/\nu = Q/(w\nu)$ the Reynolds number, and $Pe = \overline{U}h/D = Q/(wD)$ the Peclet number.

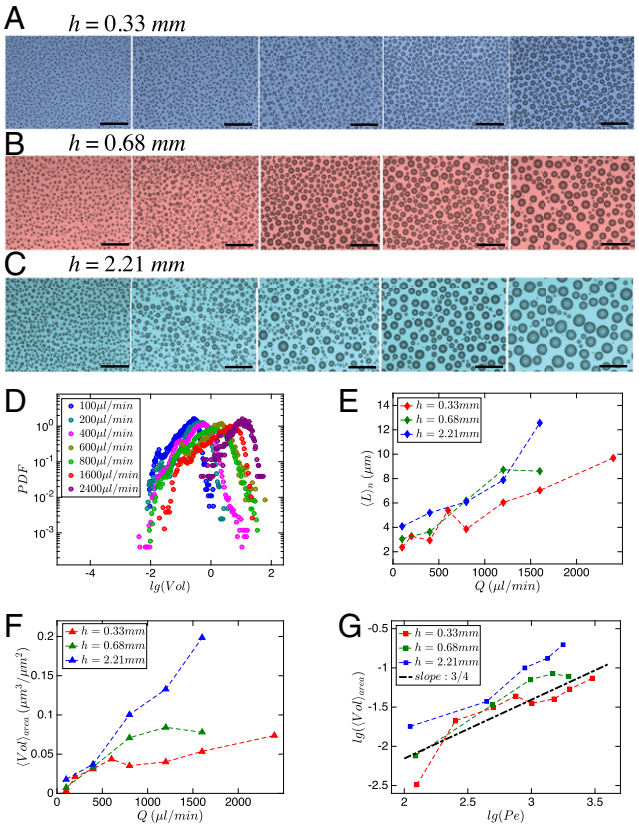

Fig. 2. Optical images and size of surface droplets formed at different flow rates in three channels. (*A*–*C*) Reflection-mode optical images of the polymerized droplets at different flow rates. (Scale bar length: 50 μm.) The flow rates were 100, 400, 800, 1,200, and 1,600 μL/min. The droplets in all of the images were polymerized after the completion of the solvent exchange. The plots show the PDF (on a logarithmic scale, reflecting that few large droplets coexist with many smaller ones) of the droplet volume produced in the narrowest channel (*D*), the averaged lateral diameter (*E*), and the averaged volume (*F*) of the surface droplets at different flow rates. (*G*) Averaged volume of droplets per μm^2 as function of the Peclet number on a log–log plot. The dashed line shows the scaling law $\langle Vol \rangle_{area} \propto Pe^{3/4}$.

strictly speaking is only justified for the narrow channel case $h = 0.33$ mm.

In principle, the solvent exchange process is described by the advection diffusion equations for the ethanol solution and water and the oil dissolved in it, with the no-slip boundary conditions on all walls. The initial conditions are such that in the left part of the channel there is no ethanol dissolved in the water, but oil up to its saturation concentration $c_{s,wat}$ in water. In the right part of the channel we have ethanol solution with dissolved oil at saturation concentration $c_{s,eth} > c_{s,wat}$. At time $t = 0$ the interface between the two parts of the flow is assumed to be sharp. From $t = 0$ on, the flow is driven by a pump such that the flow rate Q is constant. The interface will then develop a parabolic shape, corresponding to the laminar flow situation. It will smoothen out with advancing time; see the sketch in Fig. 3*A*. Note that downstream in the region which was initially filled with ethanol solution the front will hit the surface nearly parallel to the surface, due to the no-slip boundary condition. The width of the front is given by the diffusion process of oil (and ethanol) toward the water and water toward the ethanol. The boundary conditions for the oil are no-flux boundary conditions at the top and bottom wall. Once there is oil droplet nucleation, the oil concentration equals $c_{s,wat}$ at the droplet–water interface.

For nucleating and growing oil droplets the most relevant quantity is the oil oversaturation

$$\zeta(t) = \frac{c_\infty(t)}{c_s} - 1. \qquad [2]$$

As the liquid is saturated in the ethanol phase, there we have $c_\infty = c_{s,eth}$ and thus $\zeta = 0$. The same holds in the water–oil phase, $c_\infty = c_{s,wat}$ and thus also $\zeta = 0$. However, in the broadening front around the interface we have oversaturation $\zeta > 0$, as oil diffuses from the ethanol-rich phase toward the water-rich phase, in which it is less soluble. The maximum oversaturation is

$$\zeta_{max} = \frac{c_{s,eth}}{c_{s,wat}} - 1 > 0. \qquad [3]$$

At fixed position downstream (which initially is the ethanol phase) we first have no oversaturation, $\zeta = 0$. Then the front is passing by, during which $\zeta(t) > 0$ so that oil droplets can nucleate and grow. In the end the ethanol is basically fully replaced by the oil-saturated water and then again $\zeta = 0$. This front is characterized by the maximum ζ_{max} and by some temporal width τ (Fig. 3*B*). One may be tempted to argue that this temporal width τ depends on the flow velocity. However, note that independent of the flow velocity the nucleating droplets on the surface are horizontally hit by the mixing front. In fact, the velocity of the front is zero at the wall, due to the no-slip boundary condition. Therefore, in our laminar flow cell τ is independent of U and purely given by the diffusion process at the front between the oil-saturated ethanol and the oil-saturated water, suggesting $\tau \sim h^2/D$. For $h = 0.33$ mm, as in the narrow channel experiments, and $D = 1.6 \times 10^{-9} m^2/s$ we get $\tau \approx 60$ s.

Growth of a Nucleated Droplet. Once the oversaturation front passes, droplets nucleate and grow. Here we focus on an individual droplet. We assume that there is no pinning and that the contact angle θ is thus constant. The size of the droplet is characterized by its lateral extension L. Alternatively, we can use the radius of curvature R of the oil–water interface as a characterization of the droplet size, which we will do here. Then $Vol \sim R^3$ for the droplet volume, as θ is constant. Assuming different growth modes as stick–slip or stick–jump (23) would only change prefactors, but not the essence and the result of below scaling analysis.

Strictly speaking, for the droplet growth no symmetry holds: The axial symmetry, which is obeyed for a drop diffusively growing in still liquid, is broken by the flow direction. Nonetheless, to obtain the scaling relations we can still assume the diffusive growth equation even in spherical symmetry,

$$\dot{m} = 4\pi\rho_{oil} R^2 \dot{R} = 4\pi D R^2 \partial_r c\big|_R. \qquad [4]$$

[This does not hold for the prefactors, which will be geometry dependent and could be obtained by full direct numerical

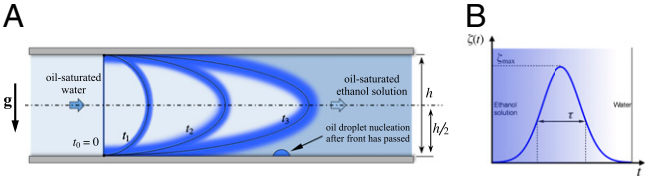

Fig. 3. (*A*) Parabolic flow profiles for various times $t \geq 0$. Note the no-slip boundary condition for the flow. The originally sharp interface will broaden with time. (*B*) Approximate temporal evolution of the oversaturation $\zeta(t)$ at fixed position downstream. The width τ of the pulse is defined through $\int_{-\infty}^{\infty} \zeta(t) dt = \zeta_{max} \tau$.

simulations, which are beyond the scope of this paper.] In this laminar flow situation the concentration gradient at the interface $\partial_r c|_R$ is given by the oil concentration difference between the oil concentration in the flow c_∞ and at the interface $c_{s,wat}$ and by the thickness λ of the concentration boundary layer, for which we assume a Prandtl–Blasius–Pohlhausen-type behavior (28, 29) as appropriate for laminar flow. Then $\lambda \sim R/\sqrt{Pe}$. That is, we have

$$\partial_r c|_R \sim \frac{c_\infty(t) - c_{s,wat}}{\lambda} \sim c_{s,wat}\frac{\zeta(t)}{\lambda} \sim c_{s,wat}\sqrt{Pe}R^{-1}\zeta(t). \quad [5]$$

Plugging this into Eq. **4** we obtain a simple ordinary differential equation for $R(t)$, namely

$$R\dot{R} \sim \frac{Dc_{s,wat}}{\rho_{oil}}\sqrt{Pe}\zeta(t), \quad [6]$$

which can easily be integrated, respectively, from 0 to the final radius R_f or from 0 to $t = \infty$, giving

$$R_f \sim \left(\frac{Dc_{s,wat}}{\rho_{oil}}\zeta_{max}\tau Pe^{1/2}\right)^{1/2}. \quad [7]$$

Here we have used $\int_0^\infty \zeta(t)dt = \zeta_{max}\tau$. Using our prior assumptions $\tau \sim h^2/D$ (in particular that it is flow rate independent) and Eq. **3** on ζ_{max}, we obtain

$$Vol_f \sim R_f^3 \sim h^3\left(\frac{c_{s,wat}}{\rho_{oil}}\right)^{3/2}\left(\frac{c_{s,eth}}{c_{s,wat}} - 1\right)^{3/2} Pe^{3/4} \quad [8]$$

for the final volume of the droplet after the solvent exchange. The scaling $Vol_f \sim Pe^{3/4}$ of our theoretical model is in good agreement with the experimental data shown in Fig. 2*G*, given that the droplet number density is flow rate independent.

Buoyancy-Driven Convection Effects for the Less-Narrow Channels

We now examine the effect of the channel height on the droplet formation. First we characterized the flow in the channels by using fluorescent microscopy, while water was dyed green to assist the visualization. Top-view movies of the entire exchange process are provided in Movies S1–S3. The snapshots in Fig. 4*A* show that in the narrowest channel the water displaced the ethanol solution in a smooth and continuous manner. The fluorescent intensity on a specific location increased with time smoothly, as the concentration of water increased in the liquid phase. The top-view snapshots in Fig. 4 *B* and C show the flow patterns for the two less-narrow channels at the same mean flow velocity $\overline{U} =$ 0.36 mm/s. Straight and regular fingers were clearly visible in the channel with $h = 0.68$ mm, whereas the flow already developed whirling patterns for $h = 2.21$ mm. The time evolution of the fluorescent intensity of the dye in water shows some deflections and jumps in the intensity, indicating the abrupt change in water content due to the nonuniform mixing. Such flow features are in contrast with the smooth flow in the narrow channel at $h = 0.33$ mm. Note that in all three cases the flow is still laminar (Table 1).

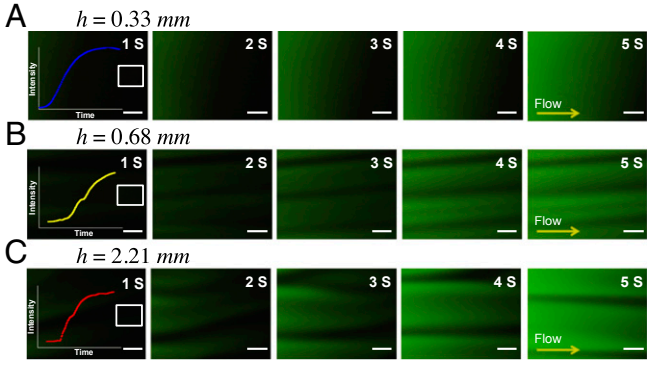

Fig. 4. Top-view snapshots of the flow during the solvent exchange in three channel heights (*A*–*C*). The direction of the water (dyed green) in the fluorescent images was from left to right. (Scale bar length: 200 μm.) The stripes for the larger h result from the convection rolls (with axes in flow direction). (*Inset*) Curve of integrated optical density of selected area as function of time as water was pushed through the channel. The mean flow velocity $\overline{U} = 0.36$ mm/s in all three channels.

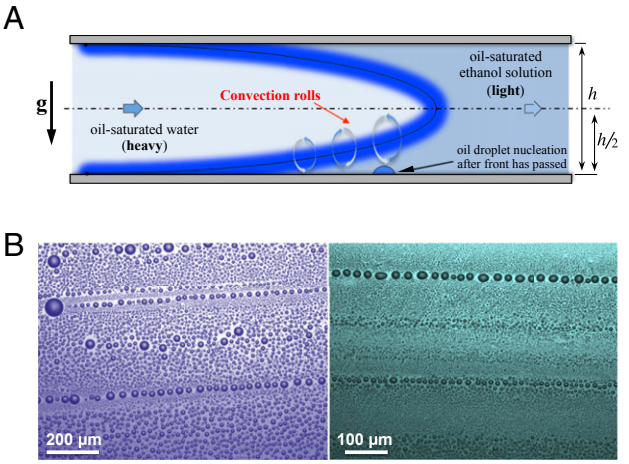

Fig. 5. Solvent exchange and nanodroplet lines in the less-narrow channels. (*A*) The illustration shows convection rolls in the bottom part of the interface between two solutions during the solvent exchange, where the heavy oil-saturated water is above the light oil-saturated ethanol aqueous solution. The axes of the roles are in flow direction, which cannot be sketched in this projection. (*B*) Two representative images of the nanodroplet lines formed in two less-narrow channels. (*Left*) $Q = 1{,}600$ μL/min and $h = 0.68$ mm. (*Right*) $Q = 400$ μL/min and $h = 2.21$ mm. The droplets organize in rows, reflecting the convection rolls with axes in flow direction. These rolls enhance mixing, leading to larger droplets where the rolls hit the substrate.

The reason for the different flow patterns in the less-narrow channels is that for them we must consider the density difference between the two miscible liquids (30, 31). The density of water is 1 g/mL whereas the density of the ethanol aqueous solution is ~0.90 g/mL. At solvent exchange, at the bottom side of the channel above the plate, the lighter ethanol will be pushed below the entraining heavier water, potentially leading to some buoyancy-driven convection rolls, with axes in flow direction. To estimate when these convection rolls set in, we can define a "Rayleigh number"

$$Ra = \frac{\Delta\rho g(h/2)^3}{\mu D_{e,w}}, \quad [9]$$

where the density difference $\Delta\rho$ is 0.1 g/mL, the gravitational acceleration g is 9.8 m/s^2, μ is the dynamic viscosity of ethanol solution, and the mass diffusion coefficient of ethanol and water $D_{e,w}$ at 300 K is 1.6×10^{-9} m^2/s. Convection only occurs at the lower half of the channel where heavy liquid (water) is above light liquid (ethanol), Fig. 5*A*. Therefore, we take $h/2$ as vertical length scale in Eq. **9**. The resulting estimated Rayleigh numbers are $\approx 1.1 \times 10^3$, 1.0×10^4, and 3.5×10^5 for the channel heights of 0.33, 0.68, and 2.21 mm, respectively. So, the convection rolls (in the top view seen as stripes) only occur in the two less-narrow channels, where the Rayleigh number is larger than the critical Rayleigh number 1,708 (32). The existence of convection rolls

for the two less-narrow channels also explains why, for fixed flow rate and thus fixed Peclet number, the average droplet size depends on the channel height, in particular for high flow rates, as seen in Fig. 2 *A*–*C*. The convection rolls lead to a better mixing between ethanol and water, and thus better transport of oil toward the substrate and consequently to larger oil droplets. Note that our scaling analysis of the previous section remains valid; only the prefactors will be affected by the convection rolls.

The development of the secondary flow at a high flow rate may lead to some patterns of the droplets. Indeed, we observed that some of the droplets produced in the least-narrow channel line up along the flow direction as shown in Fig. 5*B*. Such lines of droplets also formed at larger flow rate in the channel with $h = 0.68$ mm. They form when the convection rolls hit the surface, bringing down oil-rich liquid. All these features do not develop when we turn the channel by 90° (see the *Supporting Information*), through which we eliminate buoyancy effects.

Conclusions

In summary, we theoretically and experimentally investigated the formation of surface nanodroplets by solvent exchange under well-controlled flow conditions. We found that the flow rate and flow geometry have significant effects on the droplet size. We developed a theoretical framework for the solvent exchange process, the result of which is in good agreement with the experimental results, namely that the droplet volume increases with $Pe^{3/4}$. Increasing the channel height (for given flow rate and thus given Pe) can induce convection driven by the density difference between water and ethanol, leading to larger droplets and an inhomogeneous droplet nucleation pattern, which reflects the convection rolls. The results presented in this work provide a valuable guideline for the device design to generate surface nanodroplets with some desired sizes.

Experimental Methods

Substrate and Solutions. A stock solution containing monomer and initiator was prepared by mixing 1, 6-hexanediol di-acrylate (HDODA) (80%, Sigma-Aldrich) with 2-hydroxy-2-methylpropiophenone (97%, Sigma-Aldrich) in the ratio of 10:1. This solution of monomer precursors served as oil phase. Four mL of the monomer solution was added into 100 mL ethanol/water (50 vol %:50 vol %) solution, and the bottom phase of the liquid was the solution A. Solution B was water saturated with HDODA. The hydrophobic substrate of Si coated with monolayer of silane (octadecyltrimethylchlorosilane; OTS-Si) was prepared and cleaned by following the protocol reported in previous work (9). Before use, the OTS-Si was cleaned with chloroform, sonicated in ethanol, and dried with nitrogen. The advancing and receding contact angles of water were 112° and 98°, respectively.

Preparation, Polymerization, and Characterization of Nanodroplets. The experimental setup is shown in schematic drawing Fig. 1*A*. A flow cell was constructed by assembling a glass plate, a spacer, and a base together, forming a channel where the OTS-Si was put in. The channel height between the OTS-Si substrate and glass plate was adjusted by the thickness of the spacer. Five mL of solution A was first injected into the flow cell, followed by the injection of 10 mL solution B with a constant flow rate controlled by a syringe pump. The volume of the injected solution B was ~10× the liquid volume in the cell, which ensured solution A was fully displaced from the liquid phase. Once the droplets reached their final size, the injection of more solution B (oil-saturated water) did not further change the droplet size. After the formation of the nanodroplets, the flow cell was illuminated under a UV lamp (20 W, 365 nm) for 15 min, allowing the polymerization of the monomer droplets. The substrate was then washed with ethanol and dried by a gentle stream of nitrogen. Images of the polymerized microdroplets were acquired using a reflection-mode optical microscopy. High-resolution images of the polymerized microdroplets were also obtained from normal contact mode AFM imaging in air (Asylum Research).

ACKNOWLEDGMENTS. We thank Andrea Prosperetti for making us aware of the possible occurrence of convection rolls in this system and for very stimulating discussions, and Shuhua Peng for assisting in the experiments. X.Z. acknowledges the support from Australian Research Council (FT120100473, DP140100805); L.B. acknowledges the support from an Endeavour Research Fellowship. D.L. gratefully acknowledges the support from European Research Council (ERC) and Netherlands Center for Multiscale Catalytic Energy Conversion (MCEC).

1. Lohse D, Zhang X (2015) Surface nanobubbles and nanodroplets. *Rev Mod Phys*, in press.
2. Méndez-Vilas A, Jódar-Reyes AB, González-Martín ML (2009) Ultrasmall liquid droplets on solid surfaces: Production, imaging, and relevance for current wetting research. *Small* 5(12):1366–1390.
3. Chiu DT, Lorenz RM (2009) Chemistry and biology in femtoliter and picoliter volume droplets. *Acc Chem Res* 42(5):649–658.
4. Shemesh J, et al. (2014) Stationary nanoliter droplet array with a substrate of choice for single adherent/nonadherent cell incubation and analysis. *Proc Natl Acad Sci USA* 111(31):11293–11298.
5. Meckenstock RU, et al. (2014) Oil biodegradation. Water droplets in oil are microhabitats for microbial life. *Science* 345(6197):673–676.
6. Day P, Manz A, Zhang, Y (2012) *Microdroplet Technology Principles and Emerging Applications in Biology and Chemistry (Integrated Analytical Systems)* (Springer, New York).
7. Lou S-T, et al. (2000) Nanobubbles on solid surface imaged by atomic force microscopy. *J Vac Sci Technol B* 18(5):2573–2575.
8. Zhang XH, Ducker W (2007) Formation of interfacial nanodroplets through changes in solvent quality. *Langmuir* 23(25):12478–12480.
9. Zhang XH, et al. (2012) From transient nanodroplets to permanent nanolenses. *Soft Matter* 8(10):4314–4317.
10. Belova V, et al. (2013) Influence of adsorbed gas at liquid/solid interfaces on heterogeneous cavitation. *Chem Sci* 4:248–256.
11. Craig VSJ (2011) Very small bubbles at surfaces – the nanobubble puzzle. *Soft Matter* 7(1): 40–48.
12. Yang H, et al. (2014) Surfactant-mediated formation of polymeric microlenses from interfacial microdroplets. *Soft Matter* 10(7):957–964.
13. Vitale SA, Katz JL (2003) Liquid droplet dispersions formed by homogeneous liquid-liquid nucleation: "The ouzo effect." *Langmuir* 19(10):4105–4110.
14. Ma A, Xu J, Xu H (2014) Impact of spontaneously adsorbed hydroxide ions on emulsification via solvent shifting. *J Phys Chem C* 118(40):23175–23180.
15. Aubry J, Ganachaud F, Cohen Addad JP, Cabane B (2009) Nanoprecipitation of polymethylmethacrylate by solvent shifting: 1. Boundaries. *Langmuir* 25(4):1970–1979.
16. Lepeltier E, Bourgaux C, Couvreur P (2014) Nanoprecipitation and the "Ouzo effect": Application to drug delivery devices. *Adv Drug Deliv Rev* 71:86–97.
17. Stepanyan R, Lebouille JGJL, Slot JJM, Tuinier R, Stuart MA (2012) Controlled nanoparticle formation by diffusion limited coalescence. *Phys Rev Lett* 109(13): 138301.
18. Graužinytė M, Forth J, Rumble KA, Clegg PS (2015) Particle-stabilized water droplets that sprout millimeter-scale tubes. *Angew Chem Int Ed Engl* 54(5):1456–1460.
19. Stroock AD, et al. (2002) Chaotic mixer for microchannels. *Science* 295(5555):647–651.
20. Al-Housseiny TT, Tsai, PA, Stone, HA (2012) Control of interfacial instabilities using flow geometry. *Nat Phys* 8(10):747–750.
21. Haudin F, Cartwright JH, Brau F, De Wit A (2014) Spiral precipitation patterns in confined chemical gardens. *Proc Natl Acad Sci USA* 111(49):17363–17367.
22. Steinbock O (2014) Complexity from precipitation reactions. *Proc Natl Acad Sci USA* 111(49):17346–17347.
23. Zhang X, et al. (2015) Mixed mode of dissolving immersed nanodroplets at a solid-water interface. *Soft Matter* 11(10):1889–1900.
24. Zhang XH, Ducker W (2008) Interfacial oil droplets. *Langmuir* 24(1):110–115.
25. Schubert S, Delaney JT, Schubert, US (2011) Nanoprecipitation and nanoformulation of polymers: from history to powerful possibilities beyond poly(lactic acid). *Soft Matter* 7(5):1581–1588.
26. Yan X, et al. (2014) Simple but precise engineering of functional nanocapsules through nanoprecipitation. *Angew Chem Int Ed Engl* 53(27):6910–6913.
27. Lhuissier H, Lohse D, Zhang X (2014) Spatial organization of surface nanobubbles and its implications in their formation process. *Soft Matter* 10(7):942–946.
28. Schlichting H, Gersten K (2000) *Boundary Layer Theory* (Springer, Berlin), Vol 8.
29. Grossmann S, Lohse D (2004) Fluctuations in turbulent Rayleigh-Bénard convection: The role of plumes. *Phys Fluids* 16(12):4462–4472.
30. Lajeunesse E, Martin J, Rakotomalala N, Salin D (1997) 3D Instability of miscible displacements in a Hele-Shaw cell. *Phys Rev Lett* 79(26):5254–5257.
31. Bischofberger I, Ramachandran R, Nagel SR (2014) Fingering versus stability in the limit of zero interfacial tension. *Nat Commun* 5:5265.
32. Faber TE (1995) *Fluid Dynamics for Physicists* (Cambridge Univ Press, Cambridge, UK).
33. Prakash VN, et al. (2012) How gravity and size affect the acceleration statistics of bubbles in turbulence. *New J Phys* 14(10):105017.